Received: 11 March 2022 | Revised: 24 April 2022 | Accepted: 24 April 2022

DOI: 10.1002/cey2.229

RESEARCH ARTICLE

CARBON ENERGY WILEY

# Atmosphere-free activation methodology for holey graphene/cellulose nanofiber-based film electrode with highly efficient capacitance performance

**Heng Wu**[1] | **Wenyu Yuan**[1] | **Xiaowen Yuan**[2] | **Laifei Cheng**[1]

[1]Science and Technology on Thermostructural Composite Materials Laboratory, Northwestern Polytechnical University, Xi'an, China

[2]Future Fibres Laboratory, School of Engineering, Computer and Mathematical Sciences, Auckland University of Technology, Auckland, New Zealand

**Correspondence**
Xiaowen Yuan, Future Fibres Laboratory, School of Engineering, Computer and Mathematical Sciences, Auckland University of Technology, 6 Saint Paul St, Auckland 1010, New Zealand.
Email: xiaowen.yuan@aut.ac.nz

**Funding information**
Ministry of Business, Innovation and Employment Endeavour Fund of New Zealand, Grant/Award Number: (MAUX1801); China Postdoctoral Science Foundation, Grant/Award Number: (2021M692622)

## Abstract

An efficient chamber-induced activation method was applied for the preparation of holey graphene/cellulose nanofiber-based film with high specific surface area (SSA) and multiple channels through the graphene nanosheets. With the cellulose nanofiber (CNF) simultaneously serving as "dispersing agent," "spacer," and "activating agent," the graphene oxide (GO) nanosheets are perforated by the pyrolysis gas from CNF in the confined space inside the hybrid films, uniformly dispersed, and sandwiched between CNF networks with less agglomeration and restacking. Additionally, we have proved that $H_2O$ and $H_2$ are primarily responsible for the activation and etching of GO/CNF film. As the CNF content increases, the mesoporosity of the activated reduced GO/CNF (A-RGO/CNF) film increases, and the graphene nanosheets show more nanopore perforations. Benefitting from the high SSA, high density, moderate mesoporosity, and abundant channels for ion diffusion through the graphene nanosheets, the A-RGO/CNF film exhibits the highest specific capacitance of 323 (236) F $g^{-1}$ (F $cm^{-3}$) at 1 A $g^{-1}$. For the A-$RGO_5$/$CNF_5$ film containing half CNF and half GO, an excellent comprehensive electrochemical performance including superior rate performance (208 (160) F $g^{-1}$ (F $cm^{-3}$) at 60 A $g^{-1}$) is exhibited. Moreover, the A-$RGO_5$/$CNF_5$ electrode in an all-solid-state flexible symmetric supercapacitor delivers a high specific capacitance of 250 (193) F $g^{-1}$ (F $cm^{-3}$) at 1 A $g^{-1}$. This study provides a novel idea for the preparation of holey graphene-based film for supercapacitor electrodes. The strategy of simultaneously employing CNF as "dispersing agent," "spacer," and "activating agent" also offers a new vision for the assembly of homogeneous nanohybrid material and the utilization of pyrolysis gas.

**KEYWORDS**
cellulose nanofiber, chamber-induced activation, holey graphene, supercapacitor

## 1 | INTRODUCTION

Supercapacitors, also known as electrical double-layer capacitors (EDLCs), represent a key technology to bridge the performance gap between batteries and electrostatic capacitors.[1–3] As the electrical double-layer capacitance is formed through reversible ion adsorption/desorption inside the EDLC electrodes, a supercapacitor usually exhibits high power density, fast charge/discharge rate, and excellent cycling stability.[4,5] Nevertheless, the currently available commercial EDLCs employing activated carbons (ACs) as electrode materials typically show a much lower energy density (4–6 Wh $kg^{-1}$) when compared with conventional lead-acid batteries (25–35 Wh $kg^{-1}$).[6,7] To improve the energy density of EDLCs to meet the growing demands of energy storage and mobile power supplies, such as electric vehicles, cranes, and portable consumer electronics, a variety of novel carbon materials, including carbide-derived carbons, ordered mesoporous carbons, fullerenes, metal-organic frameworks derived carbons, biomass-derived carbons, carbon nanotubes (CNTs), and graphene, have been extensively investigated as EDLC electrode materials.[8–14]

Among various novel carbon materials, graphene has been regarded as one of the most promising materials due to its excellent electrical conductivity, thermal conductivity, electrochemical stability, ultrahigh theoretical specific surface area (SSA) of ~2600 $m^2 g^{-1}$, and ultrahigh theoretical specific capacitance (~550 F $g^{-1}$).[15–17] To date, a variety of porous graphene microstructures, including activated graphene, mesoporous graphene, and macroporous graphene foam/aerogel, have been prepared and applied to EDLC electrodes.[18–23] However, the activated graphene with abundant ultrasmall micropores usually exhibits poor rate performance due to tortuous ion diffusion channels.[24–26] Benefitting from the larger pores and wider channels, which are conducive to the rapid diffusion of ions, the mesoporous graphene as well as macroporous graphene foam/aerogel shows greatly improved rate performance.[27,28] Nevertheless, the low bulk density of these graphene foam/aerogel always leads to poor volumetric specific capacitance, which is very unfavorable when evaluating the practical performance of an EDLC. Moreover, since pristine graphene is insoluble in conventional solvents and is difficult to be dispersed, graphene oxide (GO) with good dispersion in water is always employed in practical applications to obtain graphene nanosheets through a subsequent reduction reaction.[6] Unfortunately, GO is prone to agglomeration and restacking due to the strong π-π interaction between oxygen functional groups on the GO nanosheets during the reduction process, resulting in much lower SSA for the obtained reduced GO (RGO) than the theoretical value.[29,30]

Many electroactive materials (ACs, CNTs, conductive polymers, metal oxides, etc.) have been used as "spacers" to combine with GO to prevent the agglomeration of GO nanosheets.[31–34] Nevertheless, although the agglomeration of GO has been curbed, the limited ion diffusion channels, the long path for ion diffusion along the vertical direction of graphene nanosheets, and the low packing density still limit the further improvement of rate performance and volumetric capacitance of graphene-based electrodes for EDLCs. As a result, great efforts have been devoted to creating more ion diffusion channels with shortened diffusion distances through perforating graphene nanosheets.[29,35,36] Among various attempts, $H_2O_2$ has been most often used as an oxidizing agent to etch GO nanosheets. Xu et al.[36] reported a holey graphene oxide (HGO) with abundant in-plane nanopores via $H_2O_2$ etching. Benefitting from the remarkably enhanced ion diffusion and access, the HGO-based graphene paper exhibits a high specific capacitance (283 F $g^{-1}$ at 1 A $g^{-1}$) and superior rate performance. In addition to $H_2O_2$ etching, $SnO_2$ catalytic carbon gasification was also employed to prepare graphene nanomeshes (GNMs) with quasiperiodic nanoholes from GO by Kim et al.[37] The GNM-based EDLC thus shows an outstanding rate capability and excellent cycle stability. Although superior electrochemical performance has been achieved for nanoperforated graphene electrodes, the related processes are complicated, costly, and time-consuming.

As a novel biomass nanomaterial, cellulose nanofiber (CNF) possesses a high aspect ratio, excellent mechanical properties, flexibility, and hydrophilicity.[38,39] Herein, we propose a chamber-induced activation strategy for the fabrication of holey graphene/CNF-based film with high SSA and an interconnected pore structure for high-performance EDLC electrodes. During the preparation of compact layered GO/CNF film, CNF not only acts as "dispersing agent" to uniformly separate and disperse GO nanosheets but also serves as a "spacer" to effectively prevent the GO nanosheet from agglomeration and restacking by forming hydrogen bonds with GO with the aid of abundant hydroxyl groups on the CNF surface. Moreover, CNF simultaneously acts as an "activating agent" to provide gaseous etchants ($CO_2$, $H_2O$, and $H_2$) in the subsequent pyrolysis process, creating abundant nanopores through the graphene nanosheets. As the CNF content increases, the SSA of A-RGO/CNF hybrid film decreases, while the mesoporosity increases with more in-plane nanopores on the graphene nanosheets. The laminated structure of A-RGO/CNF film optimizes the diffusion of electrolyte ions through the compact graphene nanosheets by providing abundant vertical and horizontal channels inside the A-RGO/CNF film. The A-RGO/CNF film could thus exhibit a high specific capacitance of 323 (236) F $g^{-1}$ (F $cm^{-3}$) at 1 A $g^{-1}$. When the relative content of CNF is equal to that of GO, the overall electrochemical performance of the hybrid

electrode is optimal. The A-RGO$_5$/CNF$_5$ electrode shows a superior specific capacitance of 291 (224) F g$^{-1}$ (F cm$^{-3}$) at 1 A g$^{-1}$ with 71% capacitance retention at 60 A g$^{-1}$, owing to its relatively high SSA (1583 m$^2$ g$^{-1}$), moderate mesoporosity (50.4%), and multiple channels for the efficient diffusion of electrolyte ions. In an all-solid-state symmetric supercapacitor (SSC) using polyvinyl alcohol (PVA)-KOH gel as the electrolyte, a maximum capacitance of 250 (193) F g$^{-1}$ (F cm$^{-3}$) can be achieved for the A-RGO$_5$/CNF$_5$ electrode at 1 A g$^{-1}$.

## 2 | EXPERIMENTAL SECTION

### 2.1 | Preparation of CNF

The CNF was dissociated and obtained through high-pressure homogenization of purified cellulose extracted from sisal fiber. The detailed process steps are as follows: The sisal fiber provided by Guangdong Dongfang Sisal Group Ltd., was first cut into short fibers and finely chopped using a kitchen mixer, and the fine powder was collected after passing through a 60 mesh screen. After that, a mixed solvent of ethanol and toluene ($V$:$V$ = 1:2) was used to treat the sisal fiber powder for 6 h in a Soxhlet extractor to remove impurities, such as gums and waxes, which will dissolve in organic solvents. Subsequently, the sample was bleached at 70°C for 1 h using acidified sodium chlorite solution to remove lignin; this step was repeated several times until the product (denoted as the "bleached sisal") was completely white. The obtained sample was transferred to a 6 wt% KOH aqueous solution and stirred at room temperature for 24 h, and then treated with the same solution at 80°C for 2 h to remove hemicellulose. After these treatments, the content of lignin in the sisal fiber is reduced to below 0.1 wt%, and the content of α-cellulose exceeded 85%. The product (denoted as "purified cellulose") was washed with distilled water and diluted to 0.1 wt%. The purified cellulose suspension was first treated with a shear emulsifier at 20,000 rpm for 4 h, and then transferred to a high-pressure homogenizer and treated at a pressure of 1300 bar 20 times to obtain a homogeneous CNF suspension.

### 2.2 | Fabrication of A-RGO/CNF films

Single-layer GO powder was first added to the CNF suspension (0.1 wt%) to obtain mixtures of different mass ratios (GO:CNF = 0:1, 3:7, 5:5, 7:3, and 1:0), the mixtures were then treated with an ultrasonic cleaner (400 W) for 12 h to uniformly disperse the GO nanosheets. Subsequently, the GO/CNF films were prepared by filtering the homogeneous GO/CNF suspension through a mixed cellulose ester membrane under reduced pressure. The GO/CNF films were dried at room temperature for 48 h and then peeled off the filter membrane. After they were further dried at 60°C for 24 h, the GO$_m$/CNF$_n$ ($m$:$n$ represents the mass ratio of GO to CNF), GO, and CNF films were obtained. Subsequently, the GO/CNF films with different mass ratios were converted into A-RGO/CNF films through an atmosphere-free pyrolysis method. After the GO/CNF, GO, and CNF films were respectively placed in a thermal processing furnace powered by infrared heating (BTF-1200C-RTP; AnHui BEQ Equipment Technology Co., Ltd), the air in the tube was totally replaced with high-purity $N_2$ to avoid the influence of air on the results. Subsequently, the sample was heated to 900°C at a heating rate of 10°C min$^{-1}$ and maintained for 3 h without a flowing atmosphere. During the pyrolysis process, the tube pressure was kept at around 1 atmosphere by exhausting the excess gas into a water tank using a rubber hose; the obtained products were denoted as RGO, A-RGO$_m$/CNF$_n$, and A-CNF.

### 2.3 | Preparation of all-solid-state SSC

The gel electrolyte (PVA-KOH) was prepared as follows: 5 g PVA was first dissolved into 50 mL deionized water by vigorously stirring for 2 h at 90°C. Subsequently, 5 g KOH was slowly added to the solution under continuous stirring until the solution was clear. Two pieces of the as-prepared A-RGO/CNF films were immersed into the as-obtained PVA-KOH gel for 1 h and hung for 15 min under room conditions, and this process was repeated three times. The two films were then assembled together and dried at 80°C for 12 h. The as-prepared all-solid-state flexible SSC was labeled as A-RGO/CNF//A-RGO/CNF.

### 2.4 | Material characterizations

The nitrogen adsorption–desorption tests were carried out on a Micromeritics ASAP 2460 system at 77 K. The Brunauer–Emmett–Teller surface area was calculated based on the adsorption data from a relative pressure ($P/P_0$) between 0.05 and 0.3. The pore volume and pore size distribution were obtained using the nonlocal density functional theory (NLDFT) model. The morphology of all samples was characterized by a Tescan Clara GMH field-emission scanning electron microscope (FE-SEM) and an FEI Themis Z F-30 double Cs-corrector transmission electron microscope (TEM). The X-ray diffraction (XRD)

spectra were recorded with a Bruker D8 Advance diffractometer (Cu Kα radiation, $\lambda = 1.5406$ Å). The X-ray photoelectron spectroscopy (XPS) was studied by a Thermo Scientific K-Alpha X-ray photoelectron spectrometer (Al Kα source, 1486.6 eV). The Raman spectra were obtained on a Renishaw-inVia confocal Raman microscope system using a 514.5-nm laser source. The thermogravimetric Fourier transform infrared spectroscopy (TG-FTIR) and thermogravimetric-mass spectrum (TG-MS) analysis were, respectively, carried out by a PerkinElmer TG-FTIR system (Thermal Analyzer STA 8000/FTIR Spectrometer FRIONT) and a TG-MS system (Mass Spectrometer Thermal Mass) with a heating rate of 10°C $min^{-1}$.

## 2.5 | Electrochemical measurements

The electrochemical measurements were first performed in a three-electrode system employing a platinum plate as the counter electrode, a Hg/HgO electrode as the reference electrode, and 6 M KOH solution as the electrolyte. The as-obtained film sample was directly employed as the working electrode without using conductive carbon black or organic binder. The cyclic voltammetry (CV), galvanostatic charge-discharge, and electrochemical impedance spectroscopy (EIS) measurements were all carried out using an electrochemical workstation (CHI660E; Chenhua) at room temperature. The EIS was recorded from 100,000 Hz to 0.01 Hz with an amplitude of 5 mV at open-circuit potential. Before measurements, all film electrodes were immersed in the electrolyte for 12 h. For the all-solid-state SSC, the CV and galvanostatic charge–discharge measurements were also performed at room temperature at a potential between 0 and 1.0 V. For the three-electrode system, the specific capacitance ($C_g$, F $g^{-1}$ or $C_V$, F $cm^{-3}$) of every film electrode was calculated based on the galvanostatic discharge result using the following equations:

$$C_g\,(F\,g^{-1}) = \frac{I}{(dv/dt) \times m} \tag{1}$$

$$C_V\,(F\,cm^{-3}) = \frac{I}{(dv/dt) \times V} \tag{2}$$

where $I$ (A) is the applied current, $dV/dt$ is the average slope of the galvanostatic discharge curve after ohmic drop, and $m$ (g) and $V$ ($cm^3$), respectively, represent the mass and volume of the film electrode. The capacitance ($C_g$, F $g^{-1}$ or $C_V$, F $cm^{-3}$) of the electrode in the all-solid-state SSC was calculated according to the below equations, based on the mass of electroactive material in a single electrode.

$$C_g\,(F\,g^{-1}) = \frac{2I}{(dv/dt) \times m} \tag{3}$$

$$C_V\,(F\,cm^{-3}) = \frac{2I}{(dv/dt) \times V} \tag{4}$$

The energy density $E$ (Wh $cm^{-3}$) and power density $P$ (W $cm^{-3}$) were calculated using the following equations:

$$E = \frac{C_V \times V^2}{2 \times 4 \times 3.6} \tag{5}$$

$$P = \frac{E \times 3600}{\Delta t} \tag{6}$$

where $V$ (V) represents the cell voltage after the ohmic drop and $t$ is the discharge time (s).

## 2.6 | Theoretical calculation

The electrochemical process of the electrode was simulated by COMSOL Multiphysics using the third-order current distribution. The governing equation is the Nernst–Planck equation. The electrode material is set as graphene. The voltage is set to 0.5 V (vs. reference). In the electrolyte, the concentration of $K^+$ and $OH^-$ are both set to 6.0 mol $L^{-1}$. Open boundaries are used instead of the counter electrode and the distant electrolyte. A free-triangular mesh and transient solvers are used to calculate the results.

# 3 | RESULTS AND DISCUSSION

## 3.1 | Materials characterization

The schematic diagram of the preparation process of A-RGO/CNF film is shown in Figure 1. CNF was first extracted and dissociated from sisal fiber, and the related results and discussion are shown in Figures S1–S3 and Table S1. Benefitting from the rich –OH groups in CNF and the oxygen functionalities in GO nanosheets, abundant hydrogen bonds are formed between the two components, and GO can thus be uniformly separated and dispersed in NFC networks.[40] After vacuum filtration, 1D CNF is randomly sandwiched between the 2D GO nanosheets. During the subsequent pyrolysis process, a mass of pyrolysis gases, including $H_2O$, $CO_2$, and $H_2$, all of which could function as activation agents, are continuously released from CNF and accumulated in the confined space inside GO/CNF films, finally leading to chamber-induced etching of the carbon residue derived from both GO and CNF at the higher

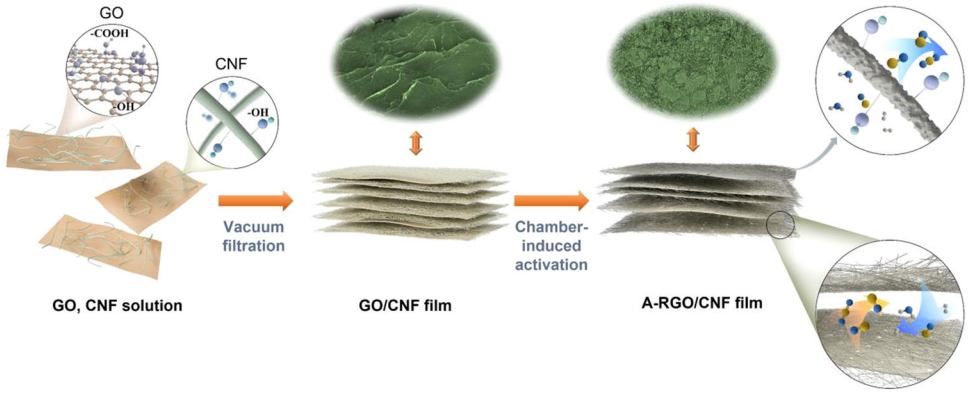


FIGURE 1 Schematic diagram of the preparation process of activated reduced graphene oxide/cellulose nanofiber (A-RGO/CNF) film.

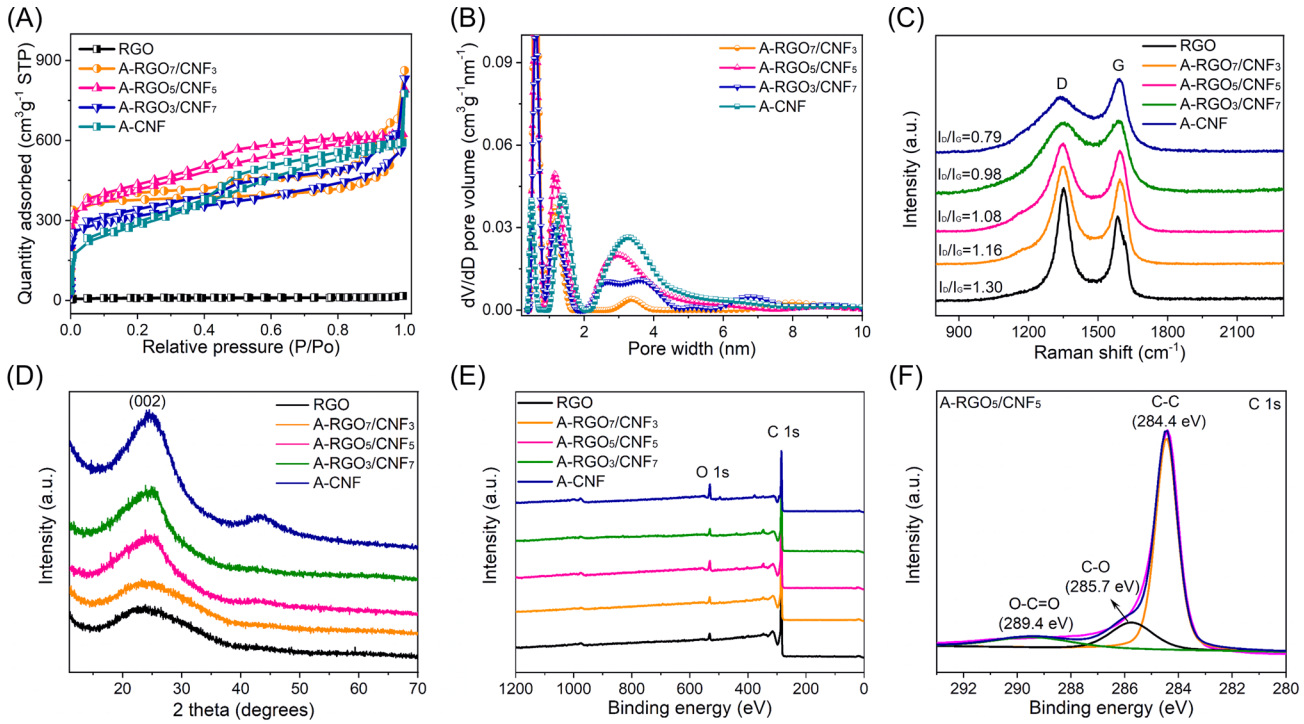


FIGURE 2 (A) Nitrogen adsorption/desorption isotherms of the RGO, A-CNF, and A-RGO/CNF at 77 K. (B) Pore size distribution of the A-CNF and A-RGO/CNF. (C) Raman spectra and (D) XRD spectra of the RGO, A-CNF, and A-RGO/CNF. (E) XPS survey spectra of the RGO, A-CNF, and A-RGO/CNF. (F) High-resolution C 1s spectra of the A-$RGO_5$/$CNF_5$. A-CNF, activated CNF; A-RGO/CNF, activated reduced graphene oxide/cellulose nanofiber; XPS, X-ray photoelectron spectroscopy; XRD, X-ray diffraction.

pyrolysis temperature. In addition to achieving significantly increased SSA, the compact graphene nanosheets are also perforated with abundant nanopores after the chamber-induced activation reaction, providing multiple channels through the A-RGO/CNF films for more effective ion diffusion.

The detailed pore structure of A-RGO/CNF samples was studied by the $N_2$ adsorption-desorption technique; the results are shown in Figure 2A,B and Table S2. For the RGO film, due to the serious stacking of GO nanosheets during the vacuum filtration process, the related flat adsorption–desorption curve (Figure 2A) shows that it has a low $N_2$ adsorption capacity when compared with other samples, and the SSA of RGO film is only 24 $m^2 g^{-1}$. For the A-$RGO_7$/$CNF_3$, A-$RGO_5$/$CNF_5$, A-$RGO_3$/$CNF_7$, and A-CNF films, they all show type I/IV hybrid isotherms with a sharp rise of plots at a relative pressure ($P/P_0$) close to 0.0 and 1.0, as well as evident type H3 hysteresis loops located at $P/P_0$ higher than 0.4, demonstrating the existence of multiscale pores due to the introduction of CNF, which simultaneously acts as "dispersing

agent," "spacer," and "activation agent" in the hybrid films.[41,42] Notably, as the relative content of CNF increases, the SSA of the corresponding sample decreases from 1624 $m^2 g^{-1}$ for A-$RGO_7$/$CNF_3$ to 1583 $m^2 g^{-1}$ for A-$RGO_5$/$CNF_5$, 1198 $m^2 g^{-1}$ for A-$RGO_3$/$CNF_7$, and 987 $m^2 g^{-1}$ for A-CNF, indicating the activation of both CNF and GO during the pyrolysis process while the activated RGO could contribute larger SSA than the activated CNF (A-CNF).

The pore structure parameters of all samples were calculated using the NLDFT method and the results are shown in Table S2. Due to the severe stacking of GO nanosheets, the total pore volume ($V_{total}$) of RGO is only 0.02 $cm^3 g^{-1}$. For the A-$RGO_7$/$CNF_3$, A-$RGO_5$/$CNF_5$, A-$RGO_3$/$CNF_7$, and A-CNF films, although the $V_{total}$ (0.74–0.83 $cm^3 g^{-1}$) does not change significantly with the increasing CNF content, the mesopore volume ($V_{meso}$) obviously increases from 0.35 to 0.62 $cm^3 g^{-1}$, thus resulting in an increase in the mesoporosity (mesopore volume contribution) from 45.4% for A-$RGO_7$/$CNF_3$ to 50.4% for A-$RGO_5$/$CNF_5$, 61.3% for A-$RGO_3$/$CNF_7$, and 74.6% for A-CNF. The results prove that the CNF is beneficial to the chamber-induced activation reaction, indicative of the "activation agent" role of CNF. Figure 2B shows the pore size distribution of the A-$RGO_7$/$CNF_3$, A-$RGO_5$/$CNF_5$, A-$RGO_3$/$CNF_7$, and A-CNF films. Clearly, all samples show multiscale pore structure with pore width centering at ~0.6, 1.1–1.4, and 2.9–3.2 nm. In particular, for the A-CNF film, pores with widths between 2 and 8 nm are exhibited, demonstrating a well-developed mesopore structure of the A-CNF.

The Raman and XRD analysis were carried out to study the crystal structure of the RGO, A-$RGO_7$/$CNF_3$, A-$RGO_5$/$CNF_5$, A-$RGO_3$/$CNF_7$, and A-CNF films. Clearly, there are two peaks in every Raman spectrum in Figure 2C, namely, the G-band at 1600 $cm^{-1}$ representing graphitic carbon and the D-band at 1340 $cm^{-1}$ representing disordered carbon and graphitic defects.[43] Due to the increase of topological disordered carbon caused by breaking the C–C bond during the thermal reduction process of GO, the intensity of the D-band on the Raman spectrum of RGO film is much higher than that of the G-band and the calculated integrated intensity ratio ($I_D/I_G$) is up to 1.30. As the relative content of CNF increases, the content of graphitic carbon in the hybrid film gradually increases and results in the intensification of the G-band. Therefore, the $I_D/I_G$ ratio continuously decreases from 1.16 for A-$RGO_7$/$CNF_3$, to 1.08 for A-$RGO_5$/$CNF_5$, 0.98 for A-$RGO_3$/$CNF_7$, and 0.79 for A-CNF. The XRD analysis of all samples further corroborated the results of the Raman spectroscopy. As shown in Figure 2D, the diffraction peak at around $2\theta = 24.5°$ corresponding to (002) reflection of graphitic carbon on the XRD spectrum strengthens and sharpens with the increase of CNF content.[44] At the same time, the diffraction peak at around $2\theta = 43.5°$ corresponding to (101) reflection of graphitic carbon gradually appears. The results of Raman and XRD analysis both prove that the A-CNF possesses more ordered carbon than the activated RGO in the hybrid film.

The XPS technique was used to analyze the surface chemical structure and elemental composition of all samples, and the results are shown in Figure 2E. After high-temperature treatment, there are only two obvious element peaks on the XPS survey spectra of various films, corresponding to C and O elements. As listed in Table S3, the estimated O content of the RGO film is 1.7 at%, which is the lowest value among all samples, proving that most of the oxygen-containing functional groups in GO could be removed after the thermal reduction process. With the increase of CNF content in the hybrid film, the O content increases from 2.4 at% for A-$RGO_7$/$CNF_3$ to 4.1 at% for A-$RGO_5$/$CNF_5$, 6.4 at% for A-$RGO_3$/$CNF_7$, and 9.5 at% for A-CNF. Based on the results of XPS and the aforementioned Raman and XRD, we can conclude that the disordered carbon produced by CNF pyrolysis is more difficult to deoxidize than GO at the same temperature, thus retaining a considerable amount of O-containing functional groups. While the relatively complete removal of O-containing functional groups after the reduction of GO leaves disordered carbon and thus results in a higher $I_D/I_G$ ratio. Moreover, the finely scanned spectrum of C 1s of A-$RGO_5$/$CNF_5$ was calibrated to 284.6 eV and fitted using the Gaussian fitting method. As is shown in Figure 2F, three peaks at ~284.4, ~285.7, and ~289.4 eV prove that the surface C atoms of A-$RGO_5$/$CNF_5$ mainly exist in the form of C–C, C–O, and O–C=O, respectively.[45] Therefore, the introduced CNF in GO film not only acts as "dispersing agent," "spacer," and "activation agent" but it also brings in abundant functional groups, such as C–O and O–C=O, which are effective in contributing additional pseudocapacitance after pyrolysis.[4] As the CNF content increases, the total amount of C–O and O–C=O groups in the A-RGO/CNF films increase as well, indicative of more active sites for pseudocapacitance.

The photograph of the $GO_5$/$CNF_5$ film and the FE-SEM images of GO, CNF, and GO/CNF films with different mass ratios are shown in Figure 3. A piece of $GO_5$/$CNF_5$ film with a thickness of 35 μm shows excellent flexibility (Figure 3A) due to the introduction of robust CNF. As the GO nanosheets were severely stacked during the film preparation process through vacuum filtration without the CNF "spacer," no graphene nanosheets can be observed from the fracture surface of GO film in Figure 3B. With the introduction of CNF, which simultaneously serves as "dispersing agent" and "spacer," the stacking and agglomeration of GO nanosheets have been largely inhibited. In the $GO_5$/$CNF_5$

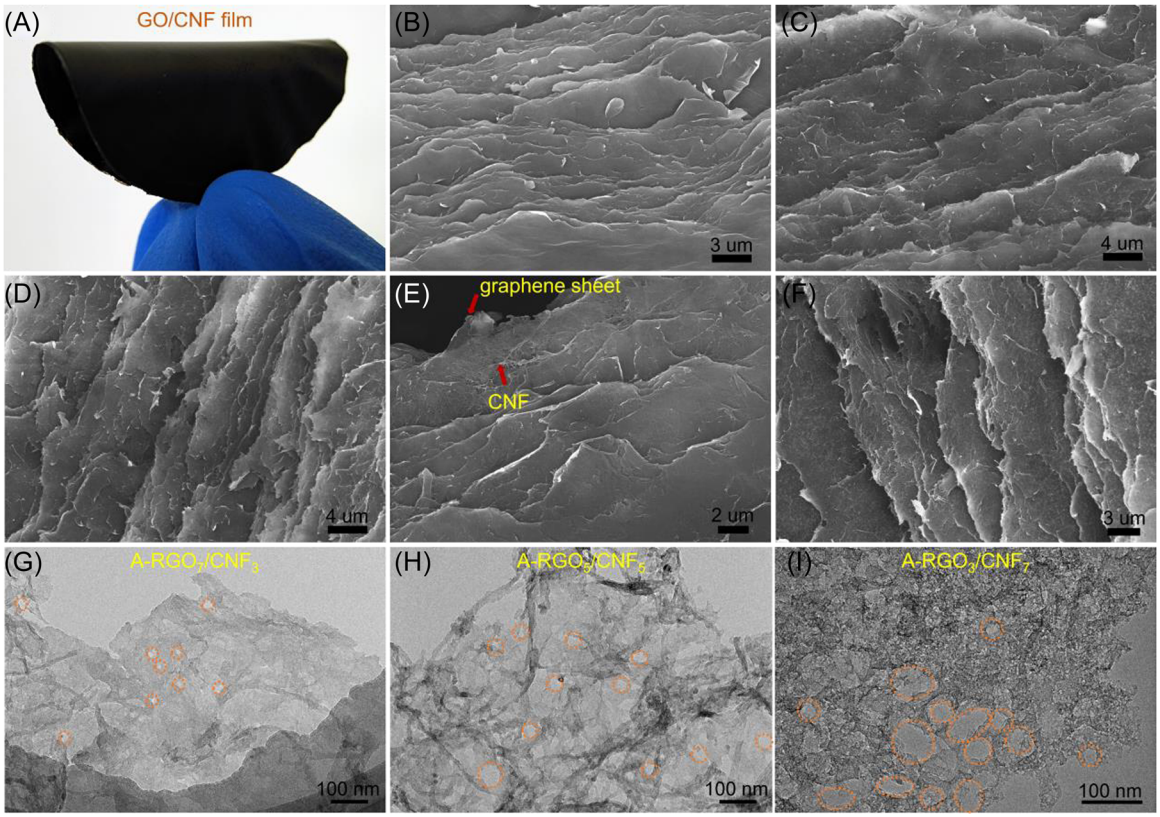


**FIGURE 3** (A) Photograph of the flexible $GO_5/CNF_5$ film with a thickness of 35 μm. SEM images of the (B) GO, (C) $GO_7/CNF_3$, (D) $GO_5/CNF_5$, (E) $GO_3/CNF_7$, and (F) CNF films. TEM images of the (G) A-$RGO_7/CNF_3$, (H) A-$RGO_5/CNF_5$, and (I) A-$RGO_3/CNF_7$ films. A-RGO, activated reduced graphene oxide; CNF, cellulose nanofiber; SEM, scanning electron microscopy; TEM, transmission electron microscope.

and $GO_3/CNF_7$ (Figure 3E) films with relatively higher content of CNF, GO nanosheets and reticular CNF are uniformly combined with each other. In the hybrid films, CNF not only prevents the agglomeration of GO nanosheets but also provides abundant interlayer channels between GO nanosheets, which are beneficial to gas diffusion during the subsequent pyrolysis and chamber-induced activation process, as well as ion diffusion in the formation of electric double-layer capacitance. Compared with the CNF sample, the size and distribution of CNF in the $GO_5/CNF_5$ and $GO_3/CNF_7$ films are more uniform, proving that CNF can also be effectively dispersed by GO. Moreover, the uniform distribution of the two components can be further verified by the TEM images (Supporting Information: Figure S4) of the $GO_5/CNF_5$ dispersion. The TEM images of the A-$RGO_7/CNF_3$, A-$RGO_5/CNF_5$, and A-$RGO_3/CNF_7$ are shown in Figure 3G–I and Figure S5. As the relative content of CNF increases, more nanofibers appear on the graphene nanosheets, which are simultaneously perforated with larger-sized nanopores, providing multiple channels inside the A-RGO/CNF films for more effective diffusion of electrolyte ions. The HRTEM images of the RGO, A-$RGO_7/CNF_3$, A-$RGO_5/CNF_5$, A-$RGO_3/CNF_7$, and A-CNF were further studied and shown in Figure S6. Compared with the RGO (Supporting Information: Figure S6A), which is composed of disordered carbon, the A-CNF (Supporting Information: Figure S6E) evidently contains abundant graphite crystallite, thus showing better graphitization. For the A-RGO/CNF films with different ratios of RGO to A-CNF (Supporting Information: Figure S6B–D), the crystalline structure of the RGO and the A-CNF almost remain unchanged. As a result, the film sample with higher content of A-CNF is believed to possess a higher graphitization degree, which is in good accordance with the results of XRD and Raman.

## 3.2 | Electrochemical performance of the A-RGO/CNF

The cyclic voltammetry (CV), galvanostatic charge-discharge, and electrochemical impedance spectroscopy (EIS) tests on the A-$RGO_7/CNF_3$, A-$RGO_5/CNF_5$, A-$RGO_3/CNF_7$, and A-CNF electrodes were first performed in a three-electrode system using 6 M KOH electrolyte to evaluate their

electrochemical performance. Figure 4A shows the CV curves of all samples at a scan rate of 100 mV $s^{-1}$. With the increase of CNF content, the mesoporosity of the film sample increases while the SSA keeps decreasing, leading to a continuously decreasing loop area. At the same time, the CV curve steadily evolves to a quasi-rectangular shape. Although the rate performance of the film electrode is improved, the specific capacitance is attenuated due to the decrease of A-RGO, which possesses a larger SSA than A-CNF. Surprisingly, for the A-$RGO_7$/$CNF_3$ electrode with the worst rate capability among all hybrid films, its CV curve still exhibits a quasi-rectangular shape representing good electric double-layer capacitance behavior at a high scan rate of 100 mV $s^{-1}$ due to the introduction of CNF.[46] The CV curves of the A-$RGO_5$/$CNF_5$ electrode at different scan rates (10–200 mV $s^{-1}$) are shown in Figure 4B. Due to the relatively high SSA (1583 $m^2$ $g^{-1}$) and moderate mesoporosity (50.4%) of A-$RGO_5$/$CNF_5$, the CV curve simultaneously exhibits a large loop area and stable shape and is not significantly deformed until the scan rate reaches 200 mV $s^{-1}$. Also, a slight deviation can be observed at the low potential of all CV curves, representing the pseudocapacitance induced by the O-containing functional groups in all electrodes.[47] The CV results show that the hybrid film electrode with higher CNF content is conducive to the formation of double-layer capacitance at every scan rate, while the greatly reduced SSA simultaneously leads to a decrease in the specific capacitance of the hybrid electrode.

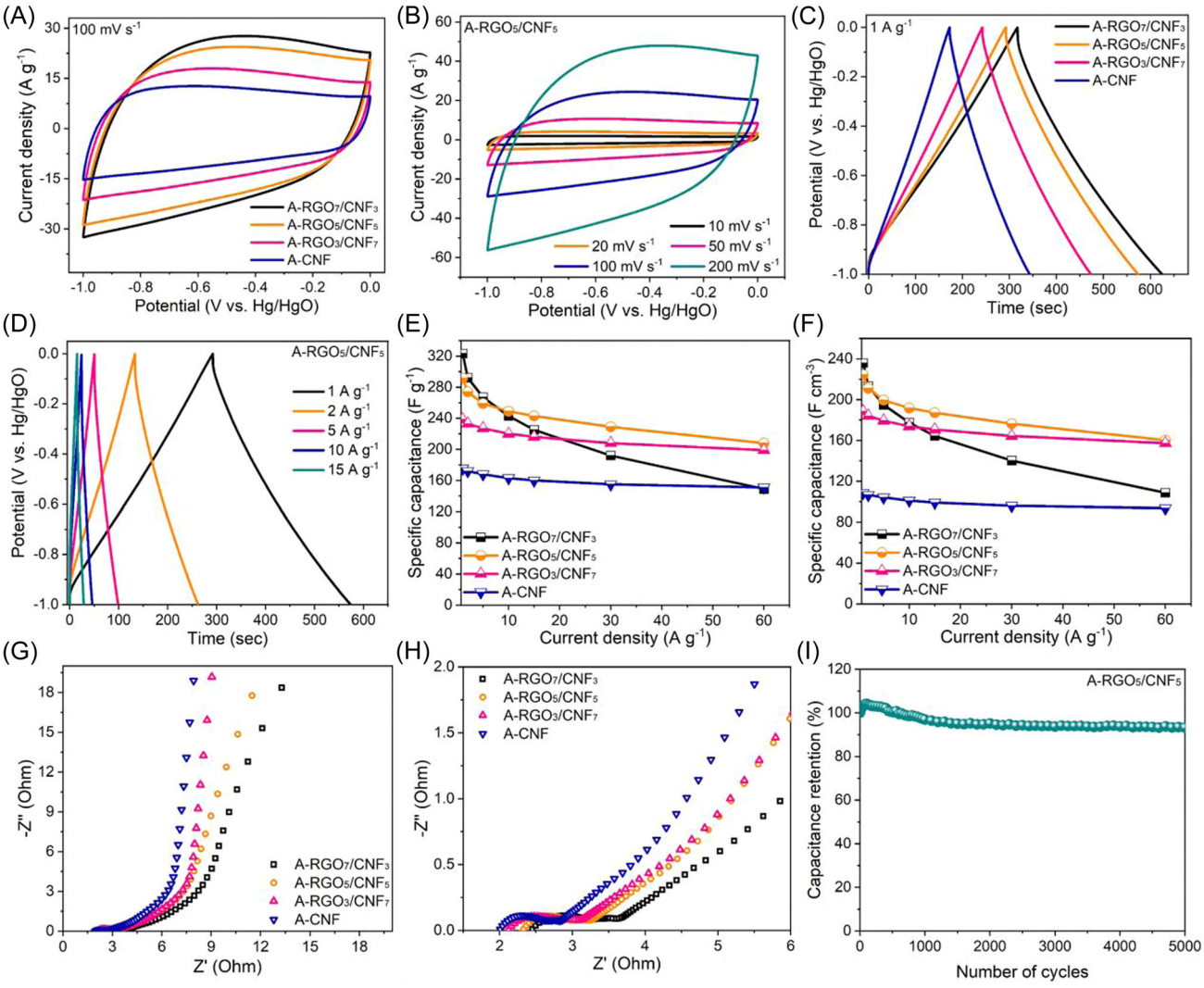


FIGURE 4 (A) CV curves of the A-CNF and A-RGO/CNF electrodes obtained at a scan rate of 100 mV $s^{-1}$. (B) CV curves of the A-$RGO_5$/$CNF_5$ obtained at scan rates ranging from 10 to 200 mV $s^{-1}$. (C) Galvanostatic charge–discharge curves of the A-CNF and A-RGO/CNF at a current density of 1 A $g^{-1}$. (D) Galvanostatic charge–discharge curves of the A-$RGO_5$/$CNF_5$ at current densities of 1–15 A $g^{-1}$. (E) Gravimetric and (F) volumetric specific capacitance of the A-CNF and A-RGO/CNF at different current densities. (G) Nyquist plots and (H) high-frequency region of the A-CNF and A-RGO/CNF electrodes. (I) Cycling performance of the A-$RGO_5$/$CNF_5$ at a current density of 10 A $g^{-1}$. A-CNF, activated CNF; A-RGO, activated reduced graphene oxide; CNF, cellulose nanofiber; CV, cyclic voltammetry.

Figure 4C shows the galvanostatic charge–discharge curves of the A-$RGO_7$/$CNF_3$, A-$RGO_5$/$CNF_5$, A-$RGO_3$/$CNF_7$, and A-CNF electrodes at a current density of 1 A $g^{-1}$. All curves clearly show a quasi-linear and symmetrical triangular shape, which represents the ideal electrical double-layer capacitance behavior of the electrodes.[48] With the increase of CNF, the discharge time continues decreasing and thus results in a rapid loss in specific capacitance. Meanwhile, the IR drop obtained from the initial stage of the discharge curve also steadily decreases from 0.051 Ω (A-$RGO_7$/$CNF_3$) to 0.049 (A-$RGO_5$/$CNF_5$), 0.042 (A-$RGO_3$/$CNF_7$), and 0.031 Ω (A-CNF), demonstrating the improved conductivity of the film electrodes. The galvanostatic charge-discharge curves of the A-$RGO_5$/$CNF_5$ electrode at different current densities (1–15 A $g^{-1}$) are shown in Figure 4D. As the current density increases, the discharge time of the A-$RGO_5$/$CNF_5$ electrode decreases while the IR drop significantly increases. Benefiting from the multiple channels through the A-$RGO_5$/$CNF_5$ films and the high mesoporosity, the diffusion resistance for electrolyte ions inside the hybrid electrode is relatively low, leading to a symmetrical charge–discharge curve even at a high current density of 15 A $g^{-1}$.

The mass-specific capacitance and the volumetric specific capacitance of the A-$RGO_7$/$CNF_3$, A-$RGO_5$/$CNF_5$, A-$RGO_3$/$CNF_7$, and A-CNF electrodes at different current densities were calculated from the discharge part of the galvanostatic charge–discharge curves and the bulk density (Supporting Information: Table S4) according to Equations (1) and (2), and the results are shown in Figure 4E,F. At a relatively low current density of 1 A $g^{-1}$, the specific capacitances of A-$RGO_7$/$CNF_3$, A-$RGO_5$/$CNF_5$, A-$RGO_3$/$CNF_7$, and A-CNF are 323 (236), 291 (224), 239 (188), and 175 (109) F $g^{-1}$ (F $cm^{-3}$), respectively. Apparently, the A-$RGO_7$/$CNF_3$ electrode with the lowest CNF content possesses the highest mass-specific capacitance and volumetric specific capacitance among all the film electrodes due to the highest SSA. As the current density gradually increases, the specific capacitance of all electrodes begins to decrease. The A-$RGO_7$/$CNF_3$ electrode with the lowest CNF content shows a rapid decrease in specific capacitance and exhibits the worst rate performance among all hybrid films; the specific capacitance of 149 (109) F $g^{-1}$ (F $cm^{-3}$) at 60 A $g^{-1}$ is 46% of that measured at 1 A $g^{-1}$. As the CNF content increases, the attenuation of the specific capacitance at higher current densities becomes unobvious due to the increasing mesoporosity, showing effectively improved rate performance. For the A-CNF electrode, the specific capacitance at a current density of 60 A $g^{-1}$ can still maintain 86% of that measured at 1 A $g^{-1}$, showing the best rate performance. Nevertheless, the specific capacitance of the A-CNF electrode at each current density is far lower than those of the A-$RGO_7$/$CNF_3$, A-$RGO_5$/$CNF_5$, and A-$RGO_3$/$CNF_7$. In particular, for the A-$RGO_5$/$CNF_5$ film composed of half GO and half CNF, it exhibited both superior specific capacitance (291 (224) F $g^{-1}$ (F $cm^{-3}$) at 1 A $g^{-1}$) and rate performance (208 (160) F $g^{-1}$ (F $cm^{-3}$) at 60 A $g^{-1}$). COMSOL Multiphysics was employed to simulate the distribution of electrolyte ions and electrons in holey graphene electrodes with different pore sizes for further understanding of the microstructure–activity relationship, and the simplified calculation model is shown in Figure S7. The specific pore sizes are approximately provided in the caption according to the TEM results in Figure 3G–I as the pore size of holey graphene cannot be accurately reflected by $N_2$ adsorption–desorption tests on the hybrid A-RGO/CNF samples. The current density distribution of holey graphene electrodes with different pore sizes is basically the same, while the pore size of holey graphene mainly affects the ion diffusion in the electrolyte. As the average pore size of holey graphene increases, $K^+$ can diffuse through the holey graphene more quickly to participate in the electrochemical behavior because wider channels are provided for ion diffusion, which is beneficial to the improvement of rate performance. On the contrary, the proportion of electroactive material decreases with the increasing pore sizes, thus resulting in decreased specific capacitance due to fewer electroactive sites. As is discussed, the theoretical calculation results are basically in accordance with the practical electrochemical performance of A-RGO/CNF electrodes with holey graphene of different pore sizes.

The EIS tests for the A-$RGO_7$/$CNF_3$, A-$RGO_5$/$CNF_5$, A-$RGO_3$/$CNF_7$, and A-CNF electrodes were performed under open-circuit voltage, and the Nyquist plots recorded in the frequency range of 0.01–$10^5$ Hz are shown in Figures 4G,H. The equivalent series resistance (ESR) of the three-electrode system is obtained from the intercept of the high-frequency region curve and the real axis. With the increase of CNF content, the ESR of the system gradually decreases from 2.45 Ω for the A-$RGO_7$/$CNF_3$ electrode to 2.33 Ω for the A-CNF electrode. As the internal resistance of the electrolyte and the interface resistance of the electrode/electrolyte are basically constant, this result reflects the gradually improving conductivity of the film electrode. As the CNF content increases, the charge transfer resistance of the electrode decreases, proving that the A-RGO/CNF film with higher conductivity and multiple channels through the graphene nanosheets possesses lower resistance of ion adsorption–desorption at the electrode interface and thus promotes charge migration. In addition, quasi-vertical lines in the low-frequency region of all Nyquist plots represent the formation of ideal electrical double-layer capacitance.[49] The Nyquist plots of A-$RGO_3$/$CNF_7$ and A-CNF show a larger slope than those of A-$RGO_7$/$CNF_3$ and A-$RGO_5$/$CNF_5$, further proving that the electrolyte ions can move more efficiently through the film electrode with multiple channels. The cycling stability

of the A-RGO$_5$/CNF$_5$ electrode was studied at a current density of 10 A g$^{-1}$. As shown in Figure 4I, the specific capacitance of the A-RGO$_5$/CNF$_5$ electrode can maintain 93.2% of the initial value after 5000 charge/discharge cycles, showing excellent cycle stability. Due to the high packing density of the A-RGO$_5$/CNF$_5$ film, the electrolyte ions slowly penetrate into the internal pores. As a result, the specific capacitance of the electrode increases slightly during the initial charge/discharge cycles; this phenomenon is also known as electrochemical activation.[50]

To further investigate the practical electrochemical performance of the A-RGO$_5$/CNF$_5$ electrode, a flexible all-solid-state SSC was assembled using the as-prepared A-RGO$_5$/CNF$_5$ as both the negative and the positive electrodes, and KOH-PVA gel as the electrolyte. Figure 5A demonstrates the CV curves of the all-solid-state SSC at different scan rates ranging from 10 mV s$^{-1}$ to 100 mV s$^{-1}$. All CV curves show quasi-rectangular shapes with no serious distortion, indicative of superior double-layer capacitive behavior. The galvanostatic charge–discharge profiles of the all-solid-state SSC obtained at different current densities from 1 to 10 A g$^{-1}$ are shown in Figure 5B, and the highly symmetrical and quasi-linear curves with no obvious voltage drop further indicate the superior electrical double-layer capacitance and the good Coulombic efficiency of the SSC. Based on the discharge profiles, the specific capacitance of the electrode at different current densities is calculated using Equations (3) and (4) and the results are shown in Figure 5C. Notably, the highest specific capacitance of 250 (193) F g$^{-1}$ (F cm$^{-3}$) is achieved at 1 A g$^{-1}$ for the A-RGO$_5$/CNF$_5$ electrode in the all-solid-state SSC. As the current density increases, the specific capacitance of the A-RGO$_5$/CNF$_5$ gradually decreases and finally reaches 181 (139) F g$^{-1}$ (F cm$^{-3}$) at a high current density of 30 A g$^{-1}$, demonstrating superior rate performance of the A-RGO$_5$/CNF$_5$ electrode due to optimized ion diffusion channels with low resistance. These values are better than those of other recently reported all-solid-state supercapacitors using graphene-based films as electrodes and are comparable to those holey graphene-based supercapacitor electrodes which are fabricated using complicated, costly, and time-consuming processes, including $H_2O_2$ etching and $SnO_2$ catalytic carbon gasification (Supporting Information: Table S5). Owing to the intrinsic stability of graphene-based electrodes, the all-solid-state SSC keeps ultrahigh capacitance retention of 94.3% after 5000 galvanostatic charge–discharge cycles, demonstrating excellent cycling stability of the device (Figure 5D). Furthermore, the flexibility of the all-solid-state SSC was investigated to evaluate its potential in wearable energy-storage devices. As

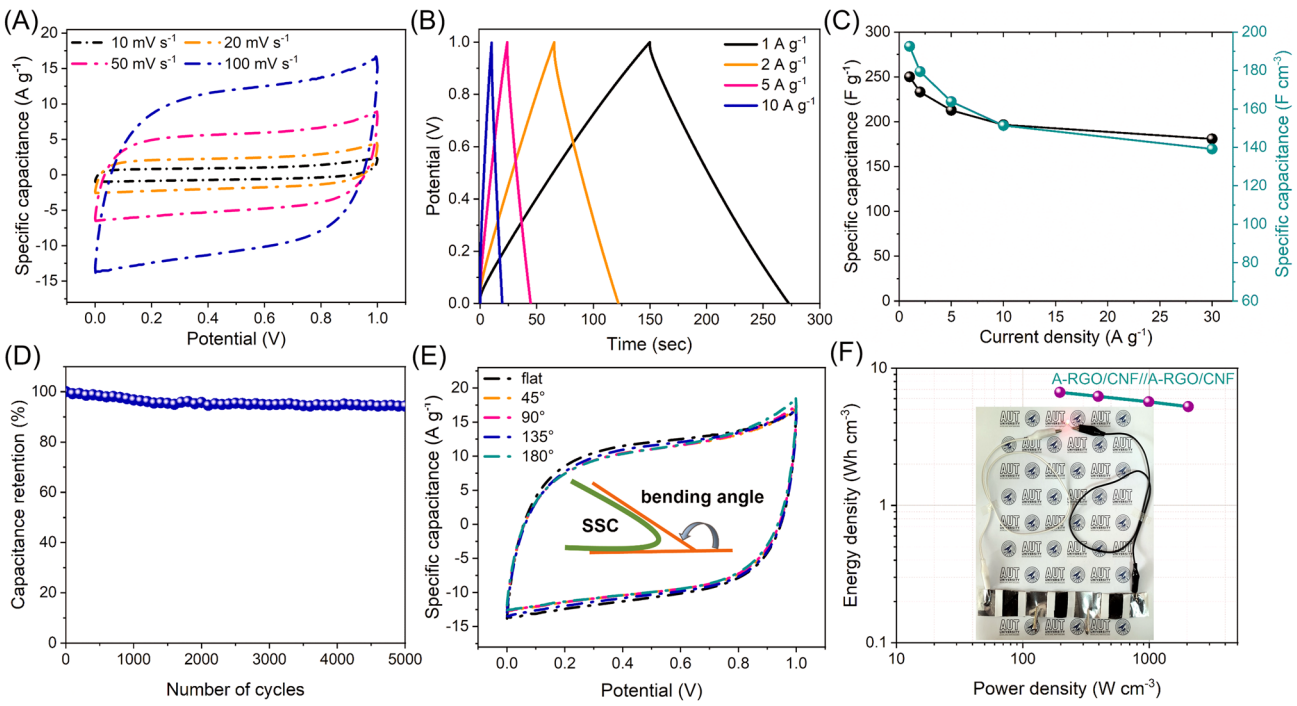


FIGURE 5 (A) CV curves of the all-solid-state SSC at different scan rates ranging from 10 to 100 mV s$^{-1}$. (B) Galvanostatic charge–discharge profiles of the all-solid-state SSC obtained at different current densities from 1 to 10 A g$^{-1}$. (C) Gravimetric and volumetric specific capacitance of the A-RGO$_5$/CNF$_5$ electrode at different current densities. (D) Cycling performance of the SSC at a current density of 10 A g$^{-1}$. (E) CV curves of the SSC under different bending angles at 100 mV s$^{-1}$. (F) Ragone plots of the A-RGO$_5$/CNF$_5$ based all-solid-state SSC. The inset in (F) shows a red LED light powered up by three A-RGO/CNF//A-RGO/CNF supercapacitors in series. A-RGO, activated reduced graphene oxide; CNF, cellulose nanofiber; CV, cyclic voltammetry; LED, light-emitting diode; SSC, symmetric supercapacitor.

is shown in Figure 5E, the CV curves of the devices capacitive behavior measured at 100 mV $s^{-1}$ remain almost the same under different bending angles, indicative of its superior flexibility and electrochemical stability. The energy density and power density of a single electrode in the SSC are estimated using Equations (5) and (6), and the results are plotted on a Ragone diagram (Figure 5F). Benefitting from the superior volumetric capacitance of the A-$RGO_5$/$CNF_5$ film electrode, the maximum power density is 2.04 kW $cm^{-3}$ at an energy density of 5.25 Wh $cm^{-3}$, while the maximum energy density reaches 6.68 Wh $cm^{-3}$ when the power density is 196.75 W $cm^{-3}$. As is shown in the inset of Figure 5F, a red light-emitting diode is illuminated by three A-RGO/CNF//A-RGO/CNF supercapacitors in series, further demonstrating the practical application of the as-prepared all-solid-state SSC.

## 3.3 | Mechanism of chamber-induced activation

TG-FTIR and TG-MS analyses were performed to study the thermal decomposition process of CNF and the changes in volatile pyrolysis gases. As shown in Figure 6A, the TG curve of CNF first enters into a zone with slight weight loss at 30–290°C due to the evaporation of absorbed water and the intramolecular dehydration.[51] After that, rapid weight loss is observed in the temperature range of 290–380°C and the weight loss of CNF in this stage can reach up to 80%.[52] The main reactions that occur in this primary degradation stage of CNF include the breakage of β-1,4 glycosidic bonds (depolymerization) and the breakage of C–O and C–C bonds of glucose monomers.[53] As the temperature continues rising, the cyclization reaction of residual char is initiated and the carbon atoms develop toward the "four-atom carbon" units and the six-membered ring-like structure. The 3D FTIR spectra in Figure 6B exhibit the evolving of pyrolysis gases from CNF during pyrolysis, as a function of both wavenumber and temperature. In the temperature range of 290–430°C corresponding to the primary degradation of CNF, a variety of volatile gases, such as $CO_2$ (~2350 $cm^{-1}$), $H_2O$ (~3400 $cm^{-1}$), and others containing chemical bonds of C–H (3100–2850 $cm^{-1}$), C–O (1300–1000 $cm^{-1}$), C═O (1900–1650 $cm^{-1}$), and C═C (1675–1640 $cm^{-1}$), are primarily detected. The release of all volatile gases reaches the maximum at around 370°C, demonstrating vigorous decomposition of CNF at this temperature. After the primary degradation stage, $CO_2$, $H_2O$, and gases containing C═O and C═C bonds are still being released until 850°C due to the further decomposition of residual char.[54] Although all kinds of volatile products, such as levoglucosan, anhydrosugar derivatives, furan derivatives, ketones, esters, and small-molecule gases, are released during the pyrolysis of CNF, to the best of our knowledge, carbon materials

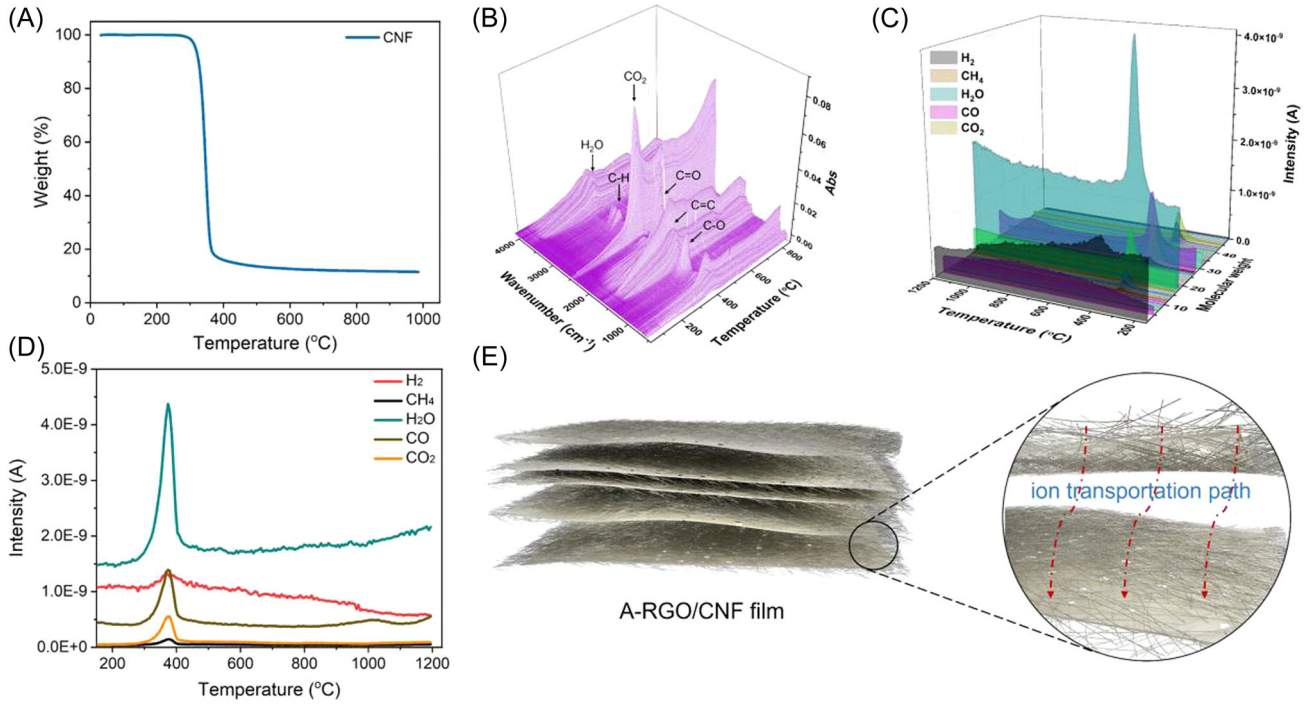


FIGURE 6 (A) TG curve of CNF. (B) 3D FTIR spectra for the pyrolysis products of CNF. (C,D) TG-MS profiles of the gas products from CNF during pyrolysis. (E) Diffusion of electrolyte ions through the graphene nanosheets. 3D, three-dimensional; CNF, cellulose nanofiber; FTIR, Fourier transform infrared spectroscopy; MS, mass spectrum; TG, thermogravimetric.

(RGO, carbonized CNF) can only be etched by $CO_2$, $H_2O$, and $H_2$ through the reactions of Equations (7), (8), and (9), respectively.[51] The TG-MS spectra in Figures 6C,D exhibit the changes of evolved gases from CNF during carbonization. As is shown, $CO_2$, $H_2O$, and $H_2$ are all detected in the gas products while $H_2O$ and $H_2$ show much higher intensity than $CO_2$, implying that Equations (8) and (9) may be the primary activation reactions. In the GO/CNF hybrid film, one dimensional (1D) CNF is compactly encapsulated by 2D GO nanosheets effectively confining the CNF. During the subsequent carbonization process of the GO/CNF film, the pyrolytic products of CNF, including $CO_2$, $H_2O$, and $H_2$, are gradually accumulated in the confined space and finally induce activation reactions to simultaneously etch both RGO and carbonized CNF at the higher pyrolysis temperature. As a consequence, the uniformly distributed compact graphene nanosheets are perforated with abundant nanopores, which function as efficient channels for the diffusion of electrolyte ions through the graphene nanosheets in the A-RGO/CNF film (Figure 6E), thus providing higher volumetric capacitance with superior rate capability when the hybrid film was employed as supercapacitor electrodes.

$$C(s) + CO_2(g) \Leftrightarrow 2CO(g) \quad (7)$$

$$C(s) + H_2O(g) \Leftrightarrow CO(g) + H_2(g) \quad (8)$$

$$C(s) + 2H_2(g) \Leftrightarrow CH_4(g) \quad (9)$$

## 4 | CONCLUSION

In summary, holey graphene-based porous A-RGO/CNF film with high SSA and efficient channels for ion diffusion was prepared from 1D CNF and 2D GO through a novel atmosphere-free activation process induced by space-confined pyrolysis of CNF. Benefitting from the unique characteristics, CNF not only acts as "dispersing agent" and "spacer" to uniformly disperse and prevent the agglomeration and restacking of GO nanosheets during the preparation of compact GO/CNF films but it also provides abundant physical activation agents, including $H_2O$, $CO_2$, and $H_2$, during its pyrolysis to simultaneously activate GO and CNF. As the released amount of $H_2O$ and $H_2$ is higher than that of $CO_2$, they may be primarily responsible for the activation of the GO/CNF films. As the content of CNF increases in the A-RGO/CNF film, the mesoporosity evidently increases, and the graphene nanosheets show more nanopore perforations. As the disordered carbon produced by CNF pyrolysis is more difficult to deoxidize than GO, a considerable amount of O-containing functional groups is left after pyrolysis, while the relatively complete removal of O-containing functional groups in GO leaves disordered carbon and thus results in a higher $I_D/I_G$ ratio. As the CNF content increases, the specific capacitance of the hybrid film electrode decreases while the rate performance is improved. The A-RGO/CNF film shows the highest specific capacitance of 323 (236) F $g^{-1}$ (F $cm^{-3}$) at 1 A $g^{-1}$. For the A-$RGO_5$/$CNF_5$ electrode composed of half GO and half CNF, an excellent comprehensive electrochemical performance, including a remarkable specific capacitance (291 (224) F $g^{-1}$ (F $cm^{-3}$) at 1 A $g^{-1}$) and superior rate performance (208 (160) F $g^{-1}$ (F $cm^{-3}$) at 60 A $g^{-1}$), is exhibited among all the A-RGO/CNF films due to its relatively high SSA (1583 $m^2$ $g^{-1}$), moderate mesoporosity (50.4%) and abundant channels for ion diffusion through the graphene nanosheets. Moreover, after assembling the A-$RGO_5$/$CNF_5$ into an all-solid-state flexible SSC using KOH-PVA gel electrolyte, the A-$RGO_5$/$CNF_5$ electrode delivers a high specific capacitance of 250 (193) F $g^{-1}$ (F $cm^{-3}$) at 1 A $g^{-1}$ with superior rate performance (181 (139) F $g^{-1}$ (F $cm^{-3}$) at 30 A $g^{-1}$). This study offers a new path for the preparation of holey graphene-based film electrodes with high SSA and efficient diffusion channels for high-performance energy storage devices.

## ACKNOWLEDGMENTS

This project was awarded and funded by the Ministry of Business, Innovation and Employment Endeavour Fund of New Zealand (MAUX1801), and supported by the China Postdoctoral Science Foundation (2021M692622).

## CONFLICTS OF INTEREST

The authors declare no conflicts of interest.

## ORCID

*Heng Wu* http://orcid.org/0000-0001-9028-6441

## REFERENCES

1. Kumar S, Saeed G, Zhu L, Hui KN, Kim NH, Lee JH. 0D to 3D carbon-based networks combined with pseudocapacitive electrode material for high energy density supercapacitor: a review. *Chem Eng J*. 2021;403:126352.
2. Chen D, Jiang K, Huang T, Shen G. Recent advances in fiber supercapacitors: materials, device configurations, and applications. *Adv Mater*. 2020;32(5):1901806.
3. Qin H, Liu P, Chen C, Cong HP, Yu SH. A multi-responsive healable supercapacitor. *Nat Commun*. 2021;12:4297.
4. Shao C, Qiu S, Wu G, et al. Rambutan-like hierarchically porous carbon microsphere as electrode material for high-performance supercapacitors. *Carbon Energy*. 2021;3(2):361-374.
5. Yin J, Zhang W, Alhebshi NA, Salah N, Alshareef HN. Synthesis strategies of porous carbon for supercapacitor applications. *Small Methods*. 2020;4(3):1900853.

6. Wu H, Zhang Y, Cheng L, et al. Graphene based architectures for electrochemical capacitors. *Energy Storage Mater*. 2016;5: 8-32.
7. Yang Z, Tian J, Yin Z, Cui C, Qian W, Wei F. Carbon nanotube- and graphene-based nanomaterials and applications in high-voltage supercapacitor: a review. *Carbon*. 2019; 141:467-480.
8. Lilloja J, Kibena-Põldsepp E, Sarapuu A, et al. Transition-metal and nitrogen-doped carbide-derived carbon/carbon nanotube composites as cathode catalysts for anion-exchange membrane fuel cells. *ACS Catal*. 2021;11(4):1920-1931.
9. Yuan W, Zhang Y, Cheng L, Wu H, Zheng L, Zhao D. The applications of carbon nanotubes and graphene in advanced rechargeable lithium batteries. *J Mater Chem A*. 2016;4(23): 8932-8951.
10. Song L, Cao X, Li L, et al. General method for large-area films of carbon nanomaterials and application of a self-assembled carbon nanotube film as a high-performance electrode material for an all-solid-state supercapacitor. *Adv Funct Mater*. 2017;27(21):1700474.
11. Lu Z, Raad R, Safaei F, Xi J, Liu Z, Foroughi J. Carbon nanotube based fiber supercapacitor as wearable energy storage. *Front Mater*. 2019;6:138.
12. Kim M, Lim H, Xu X, et al. Sorghum biomass-derived porous carbon electrodes for capacitive deionization and energy storage. *Microporous Mesoporous Mater*. 2021;312:110757.
13. Kim M, Park T, Wang C, et al. Tailored nanoarchitecturing of microporous ZIF-8 to hierarchically porous double-shell carbons and their intrinsic electrochemical property. *ACS Appl Mater Interfaces*. 2020;12(30):34065-34073.
14. Kim M, Xu X, Xin R, et al. KOH-activated hollow ZIF-8 derived porous carbon: nanoarchitectured control for upgraded capacitive deionization and supercapacitor. *ACS Appl Mater Interfaces*. 2021;13(44):52034-52043.
15. Olabi A, Abdelkareem MA, Wilberforce T, Sayed ET. Application of graphene in energy storage device-a review. *Renewable Sustainable Energy Reviews*. 2021;135:110026.
16. Zhang H, Yang D, Lau A, Ma T, Lin H, Jia B. Hybridized graphene for supercapacitors: beyond the limitation of pure graphene. *Small*. 2021;17(12):2007311.
17. Han J, Johnson I, Chen M. 3D continuously porous graphene for energy applications. *Adv Mater*. 2022;34(15):2108750.
18. El-Kady MF, Kaner RB. Scalable fabrication of high-power graphene micro-supercapacitors for flexible and on-chip energy storage. *Nat Commun*. 2013;4:1475.
19. Niu Z, Chen J, Hng HH, Ma J, Chen X. A leavening strategy to prepare reduced graphene oxide foams. *Adv Mater*. 2012; 24(30):4144-4150.
20. Zhao Y, Hu C, Hu Y, Cheng H, Shi G, Qu L. A versatile, ultralight, nitrogen-doped graphene framework. *Angew Chem Int Ed*. 2012;51(45):11371-11375.
21. Chang J, Adhikari S, Lee TH, et al. Leaf vein-inspired nanochanneled graphene film for highly efficient micro-supercapacitors. *Adv Energy Mater*. 2015;5(9):1500003.
22. Patil AM, Wang J, Li S, et al. Bilateral growth of monoclinic $WO_3$ and 2D $Ti_3C_2T_x$ on 3D free-standing hollow graphene foam for all-solid-state supercapacitor. *Chem Eng J*. 2021;421: 127883.
23. Park H, Kim JW, Hong SY, et al. Microporous polypyrrole-coated graphene foam for high-performance multifunctional sensors and flexible supercapacitors. *Adv Funct Mater*. 2018; 28(33):1707013.
24. Moreno-Fernández G, Boulanger N, Nordenström A, et al. Ball-milling-enhanced capacitive charge storage of activated graphene in aqueous, organic and ionic liquid electrolytes. *Electrochim Acta*. 2021;370:137738.
25. Yang HX, Gao RZ, Pu H, et al. Hierarchical porous activated graphene nanosheets with an ultra-high potential as electrode material for symmetric supercapacitors. *Microporous Mesoporous Mater*. 2020;306:110430.
26. Zheng C, Zhou X, Cao H, Wang G, Liu Z. Controllable synthesis of activated graphene and its application in supercapacitors. *J Mater Chem A*. 2015;3(18):9543-9549.
27. Zhu Y, Ye X, Jiang H, et al. Controlled swelling of graphene films towards hierarchical structures for supercapacitor electrodes. *J Power Sources*. 2020;453:227851.
28. Yang Z, Jia Y, Niu Y, et al. One-step wet-spinning assembly of twisting-structured graphene/carbon nanotube fiber supercapacitor. *J Energy Chem*. 2020;51:434-441.
29. Xu Y, Lin Z, Zhong X, et al. Holey graphene frameworks for highly efficient capacitive energy storage. *Nat Commun*. 2014; 5:4554.
30. Lee JH, Park N, Kim BG, et al. Restacking-inhibited 3D reduced graphene oxide for high performance supercapacitor electrodes. *ACS Nano*. 2013;7(10):9366-9374.
31. Yu D, Goh K, Wang H, et al. Scalable synthesis of hierarchically structured carbon nanotube-graphene fibres for capacitive energy storage. *Nat Nanotechnol*. 2014;9(7): 555-562.
32. Yang X, Zhu J, Qiu L, Li D. Bioinspired effective prevention of restacking in multilayered graphene films: towards the next generation of high-performance supercapacitors. *Adv Mater*. 2011;23(25):2833-2838.
33. Ye S, Feng J. Self-assembled three-dimensional hierarchical graphene/polypyrrole nanotube hybrid aerogel and its application for supercapacitors. *ACS Appl Mater Interfaces*. 2014; 6(12):9671-9679.
34. Zheng C, Zhou X, Cao H, Wang G, Liu Z. Synthesis of porous graphene/activated carbon composite with high packing density and large specific surface area for supercapacitor electrode material. *J Power Sources*. 2014;258:290-296.
35. Wang X, Lv L, Cheng Z, Jian G, Qu L. High-density monolith of N-doped holey graphene for ultrahigh volumetric capacity of Li-ion batteries. *Adv Energy Mater*. 2016;6(6):1502100.
36. Xu Y, Chen CY, Zhao Z, Lin Z, Duan X. Solution processable holey graphene oxide and its derived macrostructures for high-performance supercapacitors. *Nano Lett*. 2015;15(7):4605-4610.
37. Nokes JM, Sharma H, Tu R, et al. Scalable fabrication of micron-scale graphene nanomeshes for high-performance supercapacitor applications. *Energy Environ Sci*. 2016;9(4): 1270-1281.
38. Dang LN, Seppälä J. Electrically conductive nanocellulose/graphene composites exhibiting improved mechanical properties in high-moisture condition. *Cellulose*. 2015;22(3): 1799-1812.
39. Wang J, Ran R, Sunarso J, et al. Nanocellulose-assisted low-temperature synthesis and supercapacitor performance of reduced graphene oxide aerogels. *J Power Sources*. 2017;347: 259-269.

40. Wang Z, Tammela P, Strømme M, Nyholm L. Nanocellulose coupled flexible polypyrrole@graphene oxide composite paper electrodes with high volumetric capacitance. *Nanoscale*. 2015; 7(8):3418-3423.
41. Wu H, Yuan W, Zhao Y, Han D, Yuan X, Cheng LB. N-dual doped sisal-based multiscale porous carbon for high-rate supercapacitors. *RSC Adv*. 2019;9(3):1476-1486.
42. Li B. Nitrogen-doped activated carbon for a high energy hybrid supercapacitor. *Energy Environ Sci*. 2016;9(1):102-106.
43. Liu Y, Lu YX, Xu YS, et al. Pitch-derived soft carbon as stable anode material for potassium ion batteries. *Adv Mater*. 2020; 32(17):2000505.
44. Li W, Chen Z, Yu H, Li J, Liu S. Wood-derived carbon materials and light-emitting materials. *Adv Mater*. 2021;33(28):2000596.
45. Jiang J, Yuan J, Nie P, et al. Hierarchical N-doped hollow carbon microspheres as advanced materials for high-performance lithium-ion capacitors. *J Mater Chem A*. 2020; 8(7):3956-3966.
46. Jayaramulu K, Dubal DP, Nagar B, et al. Ultrathin hierarchical porous carbon nanosheets for high-performance supercapacitors and redox electrolyte energy storage. *Adv Mater*. 2018; 30(15):1705789.
47. Li J, Liu W, Xiao D, Wang X. Oxygen-rich hierarchical porous carbon made from pomelo peel fiber as electrode material for supercapacitor. *Appl Surf Sci*. 2017;416:918-924.
48. Choi C, Lee JA, Choi AY, et al. Flexible supercapacitor made of carbon nanotube yarn with internal pores. *Adv Mater*. 2014; 26(13):2059-2065.
49. Wu H, Cheng L, Zhang Y, Yuan W, Zheng L. Free-standing activated flax fabrics with tunable meso/micropore ratio for high-rate capacitance. *Carbon*. 2017;116:518-527.
50. Li Z, Zhang L, Amirkhiz BS, et al. Carbonized chicken eggshell membranes with 3D architectures as high-performance electrode materials for supercapacitors. *Adv Energy Mater*. 2012;2(4):431-437.
51. Li SC, Hu BC, Ding YW, et al. Wood-derived ultrathin carbon nanofiber aerogels. *Angew Chem Int Ed*. 2018;130(24):7203-7208.
52. Tang M, Bacon R. Carbonization of cellulose fibers—I. low temperature pyrolysis. *Carbon*. 1964;2(3):211-220.
53. Wu H, Fan SW, Yuan XW, Cheng LF, Deng JL. Fabrication of carbon fibers from jute fibers by pre-oxidation and carbonization. *New Carbon Mater*. 2013;28(6):448-453.
54. Li C, Ding YW, Hu BC, et al. Temperature-invariant superelastic and fatigue resistant carbon nanofiber aerogels. *Adv Mater*. 2020;32(2):1904331.

## SUPPORTING INFORMATION

Additional supporting information can be found online in the Supporting Information section at the end of this article.

**How to cite this article:** Wu H, Yuan WY, Yuan XW, Cheng LF. Atmosphere-free activation methodology for holey graphene/cellulose nanofiber-based film electrode with highly efficient capacitance performance. *Carbon Energy*. 2023;5:e229. doi:10.1002/cey2.229